

# Geophysical Research Letters<sup>®</sup>

## RESEARCH LETTER

10.1029/2021GL094758

### Key Points:

- The surfaces of the Uranian moons show evidence for resurfacing following formation and therefore may contain subsurface oceans
- Uranus's magnetic field may induce time-varying currents in these oceans that generate induced magnetic fields
- Spacecraft measurements of such induced fields could detect oceans on each of the five major moons, especially Miranda and Ariel

### Supporting Information:

Supporting Information may be found in the online version of this article.

### Correspondence to:

B. P. Weiss,  
[bpweiss@mit.edu](mailto:bpweiss@mit.edu)

### Citation:

Weiss, B. P., Biersteker, J. B., Colicci, V., Goode, A., Castillo-Rogez, J. C., Petropoulos, A. E., & Balint, T. S. (2021). Searching for subsurface oceans on the moons of Uranus using magnetic induction. *Geophysical Research Letters*, 48, e2021GL094758. <https://doi.org/10.1029/2021GL094758>

Received 22 JUN 2021  
Accepted 23 SEP 2021  
Corrected 19 AUG 2022

This article was corrected on 19 AUG 2022. See the end of the full text for details.

## Searching for Subsurface Oceans on the Moons of Uranus Using Magnetic Induction

Benjamin P. Weiss<sup>1,2</sup> , John B. Biersteker<sup>1</sup> , Vittorio Colicci<sup>1</sup> , Allison Goode<sup>1</sup>, Julie C. Castillo-Rogez<sup>2</sup>, Anastassios E. Petropoulos<sup>2</sup>, and Tibor S. Balint<sup>2</sup>

<sup>1</sup>Department of Earth, Atmospheric and Planetary Sciences, Massachusetts Institute of Technology (MIT), Cambridge, MA, USA, <sup>2</sup>Jet Propulsion Laboratory, California Institute of Technology, Pasadena, CA, USA

**Abstract** The icy moons of Uranus may contain subsurface oceans. Such oceans could be detected and characterized using measurements of magnetic fields induced by Uranus' time-varying magnetospheric field. Here we explore this possibility for Uranus's five major moons, with a focus on Ariel. We find that the magnetic field at each moon is dominated by the synodic frequency with amplitudes ranging from  $\sim 4$  nT at Oberon up to  $\sim 300$  nT at Miranda. If these bodies contain oceans with sufficient thicknesses ( $> \sim 0.4$ – $6$  km) and conductivities ( $> 2$  S m<sup>-1</sup>) even underlying relatively thick ( $\sim 50$  km) ice shells, the induced surface fields should have amplitudes exceeding the typical  $\sim 1$  nT sensitivity of spacecraft magnetometry investigations. Furthermore, the magnetic field variations at the moons span periods ranging from 1 to  $10^3$  h. These could enable long-term measurements to separately constrain ocean and ice thicknesses and ocean salinity.

**Plain Language Summary** The icy moons of Uranus may harbor subsurface oceans. These oceans may be habitable environments and tell us about the moons' formation and the evolution of their orbits. Here we explore the possibility that these oceans could be detected and characterized by magnetic field measurements from a spacecraft. In particular, the time-varying magnetic field of Uranus may generate currents in a salty ocean by the process of induction. These currents could then generate another magnetic field detectable by a spacecraft flyby. We explore this possibility by calculating the induced magnetic fields around the five largest moons of Uranus: Miranda, Ariel, Umbriel, Titania, and Oberon. We find that the spin of Uranus and the orbital motion of the moons lead to strong time-varying fields at each moon. If these moons harbor thick (several to tens of km) oceans with salinities like that of Earth's oceans, their induced fields would likely be detectable by a close spacecraft flyby. Longer term measurements from a Uranus orbiter and/or dedicated icy moon orbiter could likely constrain the ocean and ice thickness and ocean salinity.

## 1. Introduction

Ocean worlds, planetary bodies with large-scale liquid water layers (Nimmo & Pappalardo, 2016), have been discovered amongst the icy moons of Jupiter and Saturn and perhaps beyond. Ocean worlds are of great interest for several reasons. Most importantly, they are potentially habitable environments. Second, their volatile-rich interiors represent a unique end member of planetary structure. Third, they are natural laboratories for coupled tidal, orbital and thermal evolution.

The icy moons of the ice giants are likely to be major targets of upcoming spacecraft missions (e.g., Balint et al., 2020; Elder et al., 2021; Hofstadter & Simon, 2017). Here we explore the possibility of detecting and characterizing subsurface oceans on the five major moons of Uranus—Miranda, Ariel, Umbriel, Titania, and Oberon—using spacecraft magnetometry measurements from flybys and orbiters. Amongst the 27 known Uranian moons, these are the only bodies sufficiently large to likely retain liquid water today. With the possible exception of that of Oberon, their surfaces show geomorphological evidence for resurfacing following accretion which may be a signature of past or present subsurface water. We consider the approach of magnetic induction whereby a spacecraft magnetometer senses magnetic fields from electrical currents in the oceans generated by Uranus's time-varying magnetic field. We focus on Ariel since it may be the most likely amongst the major moons to have a present-day ocean and because it experiences some of the strongest variations in the Uranian field.

This work, first presented in meeting form (Weiss et al., 2020, 2021), was conducted simultaneously and independently of two complementary studies (Arridge & Eggington, 2021; Cochrane, Nordheim, et al., 2021). The former focuses more on the two outermost moons and incorporates the effects of magnetospheric currents

(Arridge & Eggington, 2021), while the latter focuses more on statistical induction forward models and the possible effects of an ionosphere and current sheet (see Cochrane, Nordheim, et al., 2021, Cochrane, Vance, et al., 2021). Our study uniquely considers the implications of recent compositional and thermal evolution models for Ariel, including the possibility of a conducting briny rocky core, for detection and characterization of its liquid interior.

## 2. Interior Structures of the Major Moons

### 2.1. Overview of the Major Moons

Uranus' major moons have radii ranging from 235.8 km (Miranda) to 788.9 km (Titania) that generally increase outwards with semimajor axis (but with a ~3% decrease from Titania to Oberon) (de Pater & Lissauer, 2015). Their orbits are near-circular (eccentricities 0.0011 to 0.0039) and largely confined to the equatorial plane of Uranus (inclinations 0.041–0.13°, except for Miranda which is 4.3°) with semimajor axes ranging from 5.1 (Miranda) to 22.8 (Oberon) Uranus radii ( $R_U$ ) (JPL Solar System Dynamics, 2021). They are not currently in mutual mean motion resonances (Ćuk et al., 2020; Tittlemore, 1990).

The moons have mass ratios of rock to ice ranging from ~0.5 to ~0.7 for all but Miranda, which has 0.3 (Hussmann et al., 2015). Their surfaces are dominated by H<sub>2</sub>O ice [possibly in the form of methane clathrates (Schenk, 1991)], while CO<sub>2</sub> has also been identified on Ariel, Umbriel and Titania (Grundy et al., 2006). With the possible exception of Oberon, their surfaces show resurfacing, variably manifested as possible deformational features related to subsurface upwellings (e.g., coronae), surface extension (e.g., grabens), and/or cryovolcanic flows (Schenk & Moore, 2020). In particular, Ariel's surface consists of lightly cratered plains with viscously relaxed craters. The plains are dissected by 2–4 km deep troughs with floors covered with possible cryovolcanic materials interpreted to be H<sub>2</sub>O ice and/or NH<sub>3</sub>-hydrates (Cartwright et al., 2020; Schenk, 1991). The ages of the moons' surfaces may be as young as 0.1–0.4 billion years for Ariel and Miranda (Zahnle et al., 2003). The heat responsible for the resurfacing of the moons may have been supplied by the gravitational energy of formation, radiogenic elements, and possibly tidal forcing (Hussmann et al., 2015).

Three main theories for the moons' origin have been proposed. First, they may have accreted out of material that condensed in a circumuranian nebula (Szulágyi et al., 2018). However, it is uncertain if this is consistent with Uranus's 98° obliquity, which is thought to be the product of giant impacts near the end of Uranus' formation (Kegerreis et al., 2018; Morbidelli et al., 2012; Rogoszinski & Hamilton, 2021; Safronov, 1966). An alternative scenario is that the moons accreted subsequently out of the ejecta disk (Ida et al., 2020; Rogoszinski & Hamilton, 2021; Slattey et al., 1991). A third possibility is that the moons formed from tidal interactions between Uranus and rings created from the disruption of cometary material [e.g., Crida & Charnoz (2012)].

In the circumuranian nebula formation by model by Szulágyi et al. (2018), the moons formed sufficiently early that they likely contained the short-lived radionuclide <sup>26</sup>Al whose decay led to heating that could have driven early volatile melting and internal differentiation. Formation from an ejecta disk would likely have occurred after the <sup>26</sup>Al heat source was exhausted and would have required tidally driven heating for moon interiors to partially melt. Lastly, following accretion in a first generation of rings, the moons could have been tidally heated during a period of high eccentricity orbits (Charnoz et al., 2011). In the latter scenario, the moons would have formed mostly undifferentiated and undergone partial melting. Neveu and Rhoden (2019a) suggested such bodies could sustain long-lived convection of brines in a porous rocky core (25% porosity).

### 2.2. Possible Interior Oceans

The moons's surface ages suggest that they are not subject to significant tidal heating at present. However, the moons may have previously passed through one or more low-order mean motion resonances that may have generated substantial heating (Chen et al., 2014; Ćuk et al., 2020; Tittlemore, 1990). Hence, the preservation of a deep relict ocean is mainly determined by the modalities of heat transfer since the moons emerged from past resonances. Considering the strong temperature-dependence of ice's thermal conductivity, the moons would freeze in a few hundred million years following a melting event in the absence of a long-term heat source [following Castillo-Rogez et al. (2019)]. Clathrate hydrates in the icy shell could significantly slow freezing of the hydrosphere (Castillo-Rogez et al., 2019; Kamata et al., 2019). The porous briny core model (Neveu & Rhoden, 2019a)

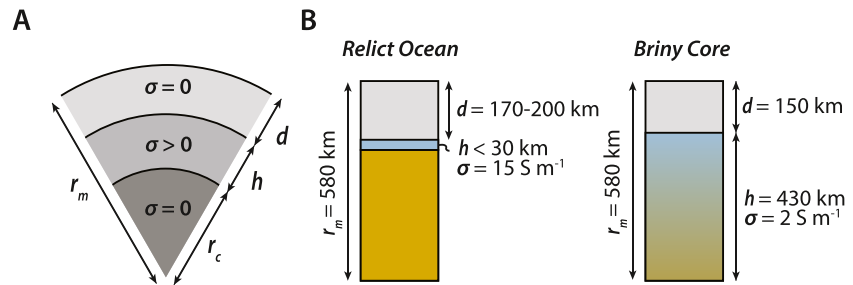


**Figure 1.** Assumed Moon interior models. (a) General model for all the moons, consisting of three-layer spherical body with a nonconducting rock ice core of radius  $r_c$ , overlain by a conducting layer of thickness,  $h$ , and conductivity,  $\sigma$ , which is in turn overlain by a nonconducting ice shell of thickness,  $d$ . (b) Two end-member spherically layered models for Ariel. Left: relict ocean, consisting of  $<30$  km-thick ocean with conductivity of  $15 \text{ S m}^{-1}$ . Right: briny core, consisting of  $430$  km-thick porous, rocky mantle with conductivity of  $2 \text{ S m}^{-1}$ .

may not allow for the presence of deep oceans in the moons except for Ariel (preliminary results by Neveu and Rhoden (2019b), whereas a clathrate-rich shell could likely maintain relict oceans in all the moons but Miranda [see also Hussmann et al., 2006]).

Given these uncertainties for the moons, we consider a broad range of interior models consisting of two and three layers with spherical symmetry (Figure 1). The three-layer model, which represents the case of a relict ocean, consists of an innermost nonconducting rocky core of radius  $r_c$  overlain by a ocean of thickness,  $h$  and uniform conductivity,  $\sigma$ , and capped with a nonconducting icy shell of thickness,  $d$  (e.g., Zimmer et al., 2000). The two-layer model, which represents the briny core case, consists of an innermost porous briny core of thickness,  $h$ , and uniform conductivity,  $\sigma$ , capped with a nonconducting ice shell of thickness,  $d$ . The outermost ice layer in both models has a radius equal to the mean radius of each moon,  $r_m$ . Mathematically, the two-layer model is an end-member of the three-layer case for which  $r_c = 0$ . Because theory and observations indicate the moons at most should have tenuous atmospheres (surface pressure  $<20$  nbar even around the largest moon, Titania), we have not included an additional outer conducting layer associated with a putative ionosphere (Widemann et al., 2009). Also, we have not included the contribution from a putative metallic core because its contribution to the induction signal is expected to be small (e.g., Zimmer et al., 2000). Analysis of these and other additional conductive layers should be the subject of future work.

For Ariel, we focus on two particular realizations of the relict ocean and briny core models that are motivated by the above considerations. For Ariel's relict ocean model, we consider a  $<30$  km-thick conductive ocean underlying a  $170$ -km thick non-conducting clathrate-rich shell. For Ariel's briny core model, we consider a solid hydrosphere overlying a briny porous rocky core (25% porosity). Both structures are consistent with Ariel's estimated ratio of rock to ice, which would indicate a total hydrosphere thickness of  $\sim 150$ – $200$  km for a differentiated body. The electrical conductivities of the conducting layers in these two cases are based on the fact that accreted volatiles such as  $\text{CO}_2$  and  $\text{NH}_3$  could significantly contribute to ocean conductivity in the form of bi/carbonate ions and ammonium. An average cometary composition would lead to an electrical conductivity of  $\sim 2 \text{ S m}^{-1}$  ( $0^\circ\text{C}$ ) prior to an increase of the salinity from freezing. A  $30$ -km thick relict hypersaline ocean could have a conductivity of  $15 \text{ S m}^{-1}$  based on terrestrial analogs (Rebello et al., 2020) and correcting for temperature effects (Smith, 1962). These are likely minimum values because we are not considering pressure effects, which tend to increase electrical conductivity at the tens of MPa pressure relevant to Ariel's residual ocean (Schmidt & Manning, 2017) and because  $<30$  km thick oceans would have even more concentrated solute. In the case of a briny core, the electrical conductivity of the mixture computed with Archie's law is of order of  $1$ – $3 \text{ S m}^{-1}$  for 30% brine mixed with rock (with the range reflecting uncertainties in brine temperature). For this study, we assume the mean value  $2 \text{ S m}^{-1}$ .

### 3. Methodology

#### 3.1. Overview of Magnetic Induction

We employ the technique of magnetic induction to search for conducting subsurface saltwater oceans (Zimmer et al., 2000). Time-varying fields inside a conducting body generate currents by Faraday's law of induction. These

currents in turn generate a secondary magnetic field by Ampere's Law that can be sensed by a magnetometer. With Ohm's law, it can be shown that the ocean current density,  $\vec{J}$ , is given by the solution to a diffusion equation:  $\nabla^2 \vec{J} = \mu_0 \sigma \left( \partial \vec{J} / \partial t \right)$  for time,  $t$ , and permeability of free space,  $\mu_0$  (Jackson, 1999).

These driving fields can be used to probe for subsurface oceans in two stages of exploration. First, detection of induced fields from at least one close (i.e.,  $< \sim 1$  moon radius in altitude) flyby could detect an ocean by measuring the induction response at a single frequency. However, degeneracies between the ocean thickness, ice thickness, and ocean conductivity make it challenging to determine these parameters separately from such single-frequency sounding. This is what the Galileo mission achieved for Europa (Zimmer et al., 2000). Second, repeated, longer-term measurements at a given moon could enable multi-frequency sounding data that could enable separate determination of the ocean thickness, ice thickness, and ocean conductivity (Seufert et al., 2011). This is the goal of the Europa Clipper mission (Raymond et al., 2015).

In the following, we begin by calculating the driving field, the time-variable field of Uranus as viewed by each moon. We will then use this to calculate the induced field. The spacecraft will measure a superposition of the steady component of the Uranian field, the driving field, and the induction field. As a metric for the feasibility of using magnetic induction to search for subsurface oceans, we will compare these fields to the nominal sensitivity of a spacecraft magnetometry investigation. For a typical spacecraft fluxgate magnetometer and/or gradiometer on  $\geq 2$  m long boom, magnetic field accuracies of  $< 1$  nT have been commonly achievable (Anderson et al., 2007; Connerney et al., 2017; Glassmeier et al., 2010; Kivelson et al., 1992).

### 3.2. Driving Field

Our goal is to calculate the magnetic field in the time and frequency domain of each moon. At the locations of the moons orbits, Uranus' magnetic field is well described by a dipole offset from Uranus' center by  $\sim 0.3 R_U$  along the spin axis toward the geographic north pole and tilted by  $59^\circ$  (Connerney et al., 1987). The wobbling of the field due to Uranus' rotation (17.2 h period), combined with orbital motion due to the moon's nonzero eccentricities and inclinations (periods ranging from 33.6 to 323 h from Miranda out to Oberon), collectively produce time variable fields in the reference frames and locations of the moons.

We calculated the moon's motions using their orbital elements (JPL Solar System Dynamics, 2021) as well as using SPICE kernels (The Navigation and Ancillary Information Facility, 2021). Because we found that both the frequencies and amplitudes of the signals with amplitudes  $> 1$  nT for both approaches were essentially indistinguishable given the accuracy of our discrete fast Fourier transform (FFT) implementation (see below), here we report just the results using the orbital elements. In the moon's reference frames,  $x$  points from the moon toward Uranus,  $y$  points opposite the direction of orbital motion, and  $z$  completes the right handed-triad (nearly along the spin axis of Uranus).

For the Uranian field, we used the internal hexadecapole  $AH_5$  magnetic field model derived from Voyager 2 Magnetometer data and Ultraviolet Spectrometer observations of aurora (Herbert, 2009) (Figure S1) at the epoch of the Voyager 2 flyby (1986). Given the estimated magnetopause distance of  $\sim 19 R_U$ , all of the moons with the occasional exception of Oberon and Titania should spend essentially all of their time within the magnetosphere (Paty et al., 2020). Furthermore, the large angle between Uranus's spin and offset dipole axes means that the moons will spend relatively little time near the magnetic equator where field perturbations associated with a magnetospheric plasma sheet could mask the induction signals (Cochrane, Vance, et al., 2021). Because we are focused on the innermost moons, we have neglected the effects of external diurnally and seasonally driven magnetospheric currents on the driving field; these are likely mainly relevant for Titania and Oberon (Arridge & Eggington, 2021) and should be the subject of future work.

We calculated the field at each moon with a frequency interval of  $0.01 \times$  the synodic frequency (i.e., time required for a moon to return to the same longitude above Uranus's surface) over a duration of  $10^7 \times$  the synodic frequency. These were chosen to minimize spectral leakage and the picket fence effect (Girgis & Ham, 1980) in the FFTs in order to accurately estimate the amplitudes of the synodic frequencies and their harmonics. We found that the highest amplitude variation is in the  $x$ -component followed by the  $y$ -component, with both components having near-zero mean and  $\sim 90^\circ$  offset in phase from one another (Figures 2 and S2). The  $z$ -component variations are

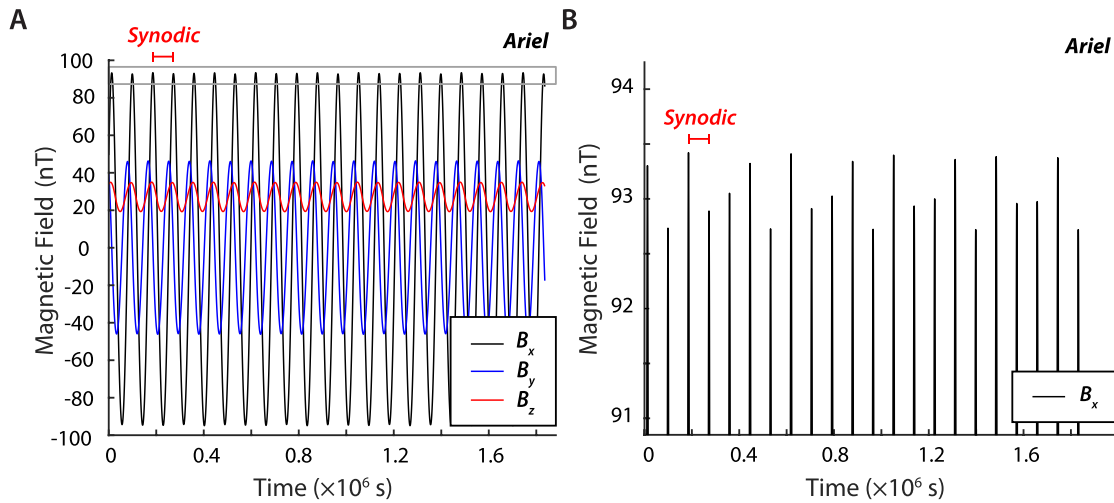


**Figure 2.** Uranus's time variable magnetic field as experienced by Ariel. (a) Three field components, where  $x$  points toward Uranus,  $y$  points opposite the orbital velocity of the moon, and  $z$  completes the triad. The synodic period is labeled. (b) Zoom-in to gray boxed region in (a), showing the presence of additional frequencies modulating and interfering with the synodic frequency.

much weaker (ranging from 14% down to 3% of that of the  $x$ -component proceeding outward from Miranda to Oberon) and with non-zero mean (Figures 2 and S2).

We find that the dominant frequency at the major moons is that of the synodic. The periods,  $T$ , and total field amplitudes,  $A$ , of the synodic variations range from  $\sim 35$  h and  $\sim 330$  nT at Miranda to  $\sim 18$  h and  $\sim 3.6$  nT out at Oberon. Furthermore, the moons experience a rich range of other driving frequencies at harmonics of the synodic frequency, their orbital frequencies, beating between the synodic and orbital frequencies, and harmonics of these frequencies (Figures 3 and S3); similar results were obtained by Cochrane, Vance, et al. (2021) and Arridge and Eggington (2021). We find that for Miranda, Ariel, and Umbriel, the first four, three and two harmonics of the synodic period, respectively, have amplitudes exceeding the nominal 1 nT magnetometry sensitivity threshold. Meanwhile, for Titania and Oberon, only the first harmonic of the synodic period exceeds this value. The orbital frequencies for all the moons are below this threshold largely due to the moons' low inclinations.

### 3.3. Induced Field

We calculate the induced field,  $B_{\text{ind}}$ , using the two and three-layer models (Figure 1) following classic techniques in electrodynamics (Jackson, 1999; Parkinson, 1983; Srivastava, 1966; Zimmer et al., 2000). Let us express Uranus's field,  $\vec{B}_U$ , as a sum of a time-independent term,  $\vec{B}_0$  and a time-variable primary field  $\vec{B}_{\text{pri}}$  that drives induction. The primary field can be expressed as the sum of  $j = 1 : N$  frequency components with amplitudes,  $\vec{B}_j$ , frequencies,  $\omega_j = 2\pi/T_j$ , and phases,  $\delta_j$ , and oriented in the direction of the unit vectors  $\vec{b}_j$  so that

$$\vec{B}_U = \vec{B}_0 + \vec{B}_{\text{pri}} = \vec{B}_0 + \sum_{j=1}^N B_j e^{-i(\omega_j t - \delta_j)} \vec{b}_j \quad (1)$$

The primary field frequencies induce oscillating dipole moments  $\vec{M}_j = -(4\pi/2\mu_0) A_j e^{i\varphi_j} B_j \vec{b}_j r_m^3$ , with amplitudes,  $A_j$  and phase lags  $+\pi + \varphi_j$  relative to that of the driving field ( $\omega_j - \delta_j$ ). The induced field is given by

$$\begin{aligned} \vec{B}_{\text{ind}} &= \sum_{j=1}^N \frac{\mu_0}{4\pi} \frac{3(\vec{r} \cdot \vec{M}_j) \vec{r} - r^2 \vec{M}_j}{r^5} \\ &= - \sum_{j=1}^N A_j e^{-i(\omega_j t - \varphi_j - \delta_j)} B_{\text{pri}} \frac{3(\vec{r} \cdot \vec{b}_j) \vec{r} - r^2 \vec{b}_j}{2r^5} r_m^3 \end{aligned} \quad (2)$$

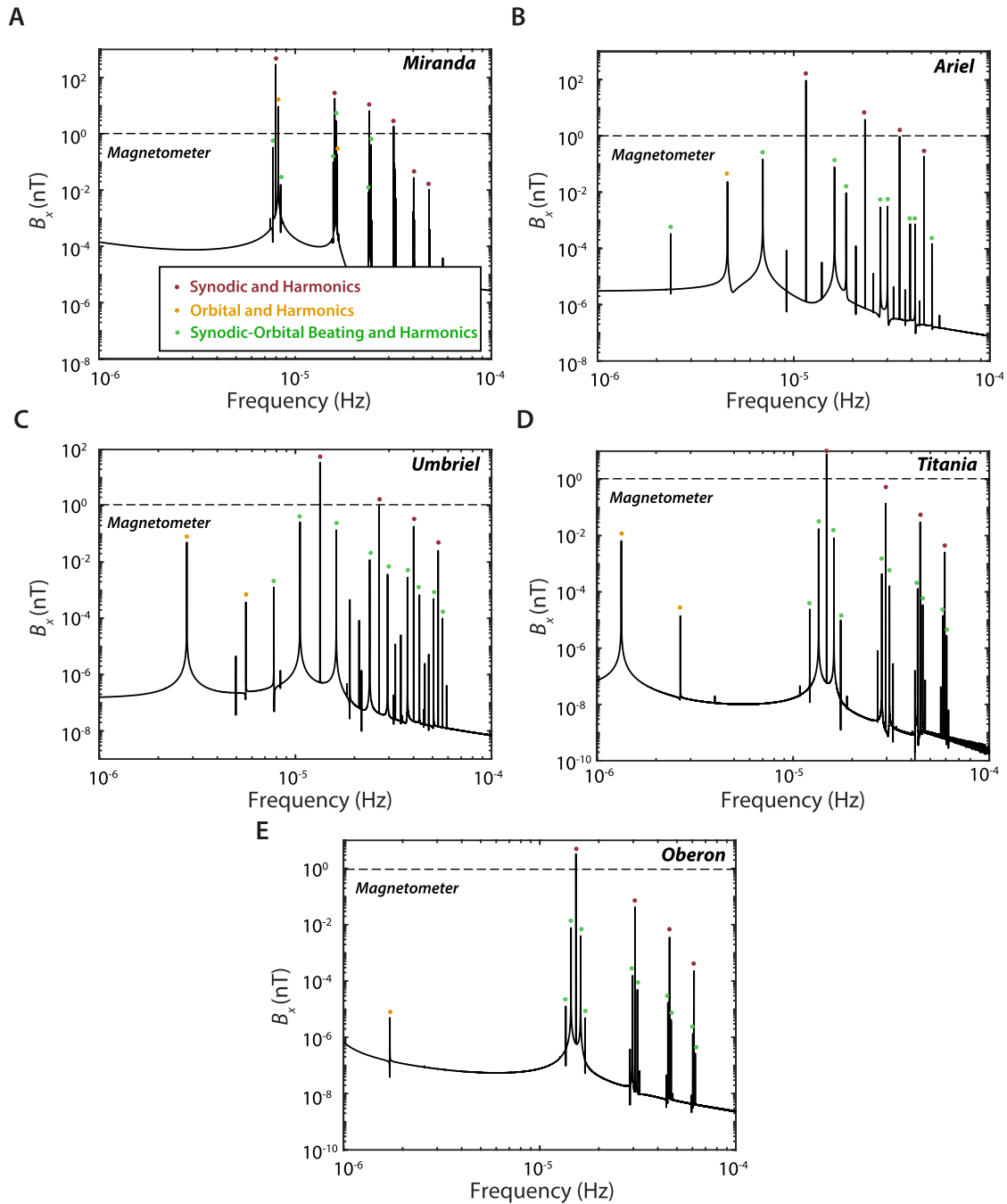


**Figure 3.** Periodogram of the  $x$ -component of Uranus's magnetic field as experienced by the major moons. There is a rich spectrum of frequencies including the synodic and its harmonics (red), the orbital frequency and its harmonics (orange), and beats between the synodic and orbital frequency harmonics (green). Dashed lines denote 1 nT sensitivity of typical spacecraft magnetometry investigations. (a) Miranda. (b) Ariel. (c) Umbriel. (d) Titania. (e) Oberon.

for radial position from the center of the moon,  $\vec{r}$ , and where

$$A_j e^{i\varphi_j} = \left( \frac{r_0}{r_m} \right)^3 \frac{R_j J_{5/2}[(r_m - d)k_j] - J_{-5/2}[(r_m - d)k_j]}{R_j J_{1/2}[(r_m - d)k_j] - J_{-1/2}[(r_m - d)k_j]} \quad (3)$$

with



$$R_j = \frac{[(r_m - d - h)k_j]k_j J_{-5/2}[(r_m - d - h)k_j]}{3J_{3/2}[(r_m - d - h)k_j] - [(r_m - d - h)k_j]k_j J_{1/2}[(r_m - d - h)k_j]} \quad (4)$$

Here,  $J_m$  are Bessel functions of the first kind and order  $m$  and  $k_j = \sqrt{i\omega_j \mu_0 \sigma}$ . For the three-layer sphere (i.e.,  $r_m - d - h > 0$ ),  $R_j$  is in general nonzero, whereas for the two-layer sphere (i.e.,  $r_m - d - h = 0$ ),  $R_j = 0$ .

The skin depth, the depth at which the primary field declines by a factor of  $1/e$  for a semi-infinite conducting half space, is given by  $s = \sqrt{2/\omega_j \mu_0 \sigma}$ . The induction amplitude grows and the phase delay shrinks as the ocean gets thicker (i.e.,  $h$  increases) and/or more conductive ( $\sigma$  increases). When the skin depth approaches the ocean thickness (i.e.,  $h \approx s$ ), the amplitude and phase lag pass through local maximum and minimum, respectively (Hand & Chyba, 2007). Eventually, as these two parameters increase further, a saturated state is reached with  $A_j = 1$  and  $\phi_j = 0$ . For thin oceans (i.e.,  $h \ll r_m$ ), Equations 3 and 4 reduce to

$$A_j \approx \frac{2r_m h}{3s^2} = \frac{\mu_0 r_m h \omega_j \sigma}{6} \quad (5)$$

Therefore, all other parameters being fixed, larger moons and higher frequency driving fields produce higher amplitude induced fields.

Forward modeling the induction field (Equation 2) consists of choosing values for  $h$ ,  $\sigma$ , and  $d$  and computing  $A_j$  and  $\phi_j$  using Equations 3 and 4. The inverse problem of solving for the three parameters  $h$ ,  $\sigma$ , and  $d$  from the two observations  $A_j$  and  $\phi_j$  at a single frequency is clearly nonunique. This is illustrated by the fact that a thick, low conductivity ocean will produce a similar amplitude induction field as a thin, conductive ocean (Khurana et al., 2009; Seufert et al., 2011). Furthermore, a thick ice shell and thick ocean will have a similar amplitude induction field as that of a thin ice and thin ocean (although the phase lag for the latter will be greater). The nonuniqueness can be broken by sounding at multiple frequencies, provided that the ocean is near saturation (i.e.,  $h \approx s$ ) for at least one of the frequencies.

## 4. Results

Because most of the variation at the synodic frequency at each moon occurs in the  $x$ - and  $y$ -components, the induction poles for these frequencies lie within  $\pm \sim 4^\circ$  of the equators of all moons but that of Miranda (for which it lies with  $\pm \sim 6^\circ$ ). The induction poles sweep across the moons with the associated induced moments oscillating in magnitude at their respective frequencies. This means that spacecraft flybys with closest approaches near the equatorial regions of the moons and that sample a widely distributed range of phases will enable the most sensitive induction studies.

The amplitude of induced fields depend on  $\sigma$ ,  $d$ , and  $h$  while the phase depends on  $\sigma$ ,  $d$ . The response exhibits a degeneracy in which a given measured amplitude and phase are each consistent with a wide range of combinations of  $\sigma$  and  $h$  (Figure 4a). The amplitude grows and the phase lag approaches 0 with increasing  $h$  (as more fluid can participate in the induction process) and increasing  $\sigma$  (as a given ocean approaches saturation) (Figures 4b and 4c). In particular, the 35–18 h range of synodic periods from Miranda out to Oberon have skin depths of  $\sim 33$ – $46$  km and  $\sim 91$ – $130$  km for oceans with conductivities like that expected for the relict ocean and briny core scenarios, respectively. Following Equation 5, the minimum ocean conductivity and thickness required to generate a 1-nT amplitude induction field at the surface induction pole grows monotonically with the moons' distance from Uranus (and therefore with the amplitude of Uranus' field), with the exception that the order of Ariel and Miranda are reversed because of Ariel's  $2.5\times$  larger radius (Figure 4a).

We first consider the case of ocean detection. We see that for the estimated conductivities of a relict ocean and briny core, surface measurements could detect conducting layers with minimum thicknesses  $< 1$  km and  $< 1$  km (for Miranda) and ranging up to  $< 1$  and  $\sim 6$  km (for Oberon), respectively under a nominal 50-km thick ice shell (Figure 4a). By comparison, oceans  $< 1$  km are detectable at Jupiter's moon Europa; this is much smaller than that of the Uranian moons mainly because of Europa's large radius (twice that of Titania) and because it experiences a large synodic amplitude approaching that of Miranda (Figure 4a). Furthermore, for a single flyby of Ariel within 200 km of its surface [e.g., that proposed for insertion of a flagship mission into orbit around Uranus

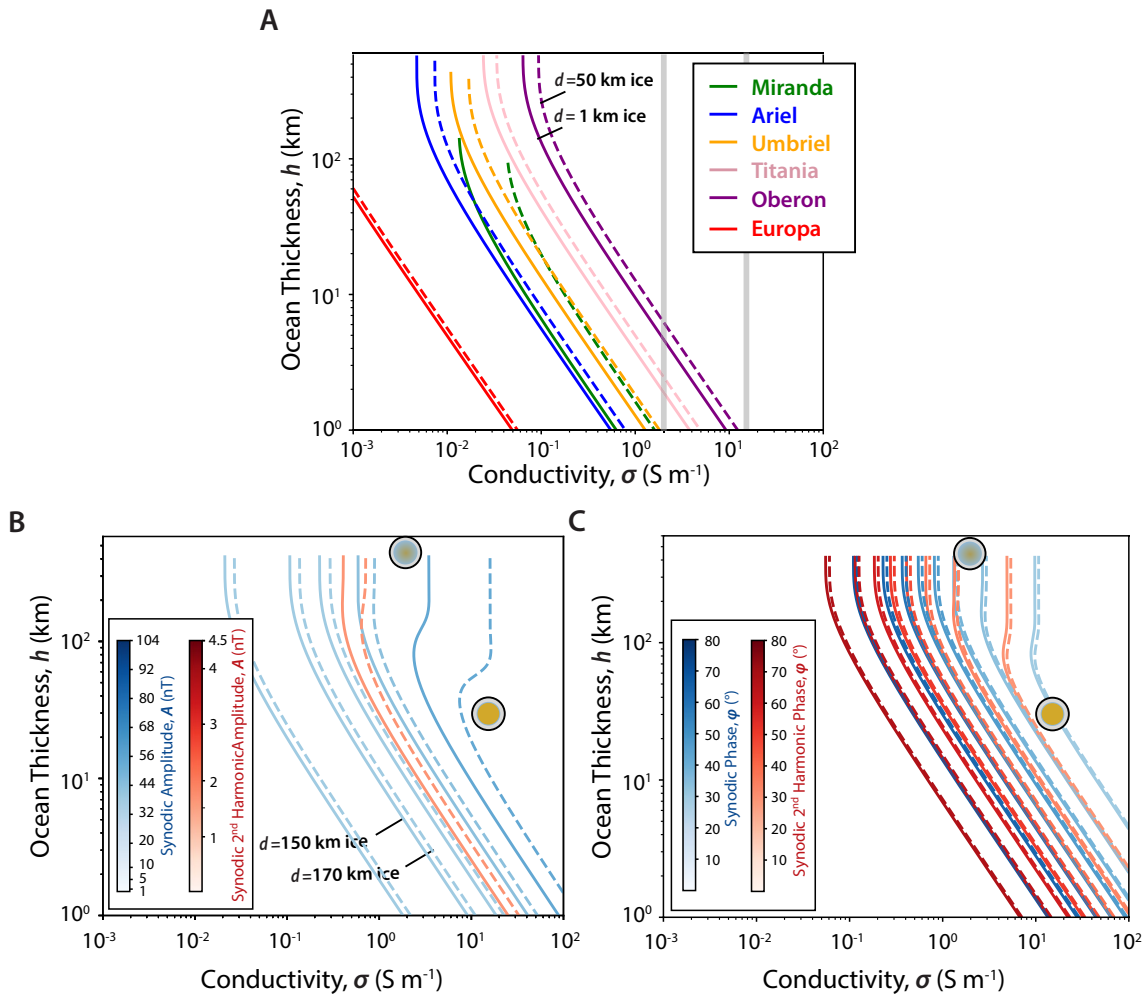


**Figure 4.** Induction fields at the synodic frequencies of the major moons and the Jovian moon Europa at the surface induction pole. (a) Combinations of ocean thickness and conductivity for producing a 1 nT amplitude. Solid and dashed curves are for ice thicknesses of 1 km (solid lines) and 50 km (dashed lines). Shown are conditions for Miranda (green), Ariel (blue), Umbriel (orange), Titania (pink), Oberon (purple), and Europa (red). Vertical gray bars denote conductivities for briny mantle (left) and relict (ocean). (b and c) Amplitude and phase of the response of the induced field for Ariel as function of ocean thickness and conductivity compared to two expected interior structures. Dashed curves denote end-member relict ocean, consisting of 30 km-thick ocean with conductivity of 15  $\text{S m}^{-1}$ , overlain by a 170-km thick ice shell. Solid curves denote briny mantle, consisting of 430 km-thick porous, conducting core with conductivity of 2  $\text{S m}^{-1}$  overlain by 150-km thick ice shell. Shown is the response to the first (red) and second (blue) harmonics of the synodic frequency. Numerical values of contours correspond to labeled values on colorbars. Two colored circles denote briny core (top) (Figure 1b) and 30-km thick relict ocean (bottom) (Figure 1c). Note that electrical conductivities greater than 20  $\text{S m}^{-1}$  are not expected even for hypersaline solutions due to interactions between ions and the low eutectic temperature of relevant solutions.

(Hofstadter & Simon, 2017)], we find that induced fields for relict oceans of thickness of just a few km as well as from the briny core should have amplitudes detectable with a typical magnetometry investigation (Figure S4). Likewise, Cochrane, Vance, et al. (2021) have shown that even in the presence of a model ionosphere, a relict ocean with just 2  $\text{S m}^{-1}$  conductivity and thickness of <10 km could be detectable.

With respect to ocean characterization, we find that multi-frequency sounding for thick and/or highly conducting oceans is likely achievable at least at Miranda and Ariel. In particular, separate determination of ocean thickness, ice thickness and ocean conductivity for Ariel may be possible for conductivities  $>\sim 1$   $\text{S m}^{-1}$  and ocean thicknesses  $>\sim 20$  km (Figures 4b and 4c). Such an investigation could be enabled by multiple flybys of each moon and/or dedicated moon orbiters or landers. For lower conductivities and ocean thicknesses, these two parameters will likely be degenerate.



## 5. Conclusions

The five major moons of Uranus may harbor relict oceans and/or briny cores underneath their ice shells. The time-variable Uranian magnetospheric field of Uranus could produce substantial induced magnetic fields in the liquid layers of these moons, dominantly at the synodic frequency and its harmonics. For a nominal 50-km thick ice layer, relict oceans layers with conductivities of  $>2 \text{ S m}^{-1}$  that have thicknesses  $>\sim 0.4\text{--}6 \text{ km}$  could be detected on the major moons by near-surface magnetic field measurements from a typical spacecraft magnetometry experiment. Multi-frequency sounding from flybys could in principle characterize the ocean thickness and conductivity for at least Miranda and Ariel. As such, searching for subsurface oceans on the major moons using magnetic induction should be a key science objective of a future mission to the Uranian system.

## Conflict of Interest

The authors declare no conflicts of interest relevant to this study

## Data Availability Statement

No data were created for this research.

## Acknowledgments

The authors thank Marc Neveu for helpful discussions. The authors thank the NASA Jet Propulsion Laboratory (JPL) (consulting services agreement #1662407), the NASA Europa Clipper project (University of Michigan/JPL SUBK00011438), the MIT Undergraduate Research Opportunities Program and the MIT Department of Earth, Atmospheric and Planetary sciences for support. Part of this work was carried out at the Jet Propulsion Laboratory under a contract with the National Aeronautics and Space Administration (80NM0018D0004). B. P. Weiss and J. B. Biersteker conceived the project, B. P. Weiss supervised the project, and all authors conducted calculations were involved in writing the manuscript.

## References

- Anderson, B. J., Acuña, M. H., Lohr, D. A., Scheifele, J., Raval, A., Korth, H., & Slavin, J. A. (2007). The magnetometer instrument on MESSENGER. *Space Science Reviews*, 131, 417–450. <https://doi.org/10.1007/s11214-007-9246-7>
- Arridge, C. S., & Eggington, J. W. B. (2021). Electromagnetic induction in the icy satellites of Uranus. *Icarus*, 367, 114562. <https://doi.org/10.1016/j.icarus.2021.114562>
- Balint, T. S., Atkinson, D., Babuscía, A., Baker, J., Bradford, C., Elder, C., et al. (2020). *Uranus System Exploration Under the New Frontiers Mission Class (A Novel Perspective)*. Retrieved from <https://baas.aas.org/pub/2021n4i040/release/1?readingCollection=7272e5bb>
- Cartwright, R. J., Beddingfield, C. B., Nordheim, T. A., Roser, J., Grundy, W. M., Hand, K. P., et al. (2020). Evidence for ammonia-bearing species on the Uranian satellite Ariel supports recent geologic activity. *The Astrophysical Journal Letters*, 898, L22. <https://doi.org/10.3847/2041-8213/aba27f>
- Castillo-Rogez, J., Hesse, M., Formisano, M., & Sizemore, H. G. (2019). Conditions for the preservations of brines inside Ceres. *Geophysical Research Letters*, 46, 1963–1972.
- Charnoz, S., Crida, A., Castillo-Rogez, J. C., Lainey, V., Dones, L., Karatekin, O., et al. (2011). Accretion of Saturn's mid-sized moons during the viscous spreading of young massive rings: Solving the paradox of silicate-poor rings versus silicate-rich moons. *Icarus*, 216, 535–550. <https://doi.org/10.1016/j.icarus.2011.09.017>
- Chen, E. M. A., Nimmo, F., & Glatzmaier, G. (2014). Tidal heating in icy satellite oceans. *Icarus*, 229, 11–30. <https://doi.org/10.1016/j.icarus.2013.10.024>
- Cochrane, C., Nordheim, T. A., Vance, S. D., Styczinski, M., Soderlund, K. M., Elder, C. M., et al. (2021). In search of subsurface oceans within the moons of Uranus. In *Lunar and Planetary Science Conference*, LII, abstract #1559.
- Cochrane, C. J., Vance, S. D., Nordheim, T. A., Styczinski, M., Masters, A., & Regoli, L. H. (2021). In search of subsurface oceans within the Uranian moons. *arXiv*. Retrieved from <https://arxiv.org/abs/2105.06087>
- Connerney, J. E. P., Acuña, M. H., & Ness, N. F. (1987). The magnetic field of Uranus. *Journal of Geophysical Research*, 92, 15329–15336. <https://doi.org/10.1029/ja092ia13p15329>
- Connerney, J. E. P., Benn, M., Bjarno, J. B., Denver, T., Espley, J., Jorgensen, J. L., et al. (2017). The Juno Magnetic Field Investigation. *Space Science Reviews*, 213, 39–138. <https://doi.org/10.1007/s11214-017-0334-z>
- Crida, A., & Charnoz, S. (2012). Formation of regular satellites from ancient massive rings in the solar system. *Science*, 338, 1196–1199. <https://doi.org/10.1126/science.1226477>
- Ćuk, M., El Moutamid, M., & Tiscareno, M. S. (2020). Dynamical history of the Uranian system. *The Planetary Science Journal*, 1, 22.
- de Pater, I., & Lissauer, J. J. (2015). *Planetary Sciences* (2nd ed.). Cambridge, UK: Cambridge University Press.
- Elder, C. M., Nordheim, T. A., Pathoff, D. A., Leonard, E., Cartwright, R. J., Cochrane, C., et al. (2021). Uranus magnetosphere and moons investigator. In *Lunar and Planetary Science Conference*, LII, abstract #2289.
- Girgis, A., & Ham, F. M. (1980). A quantitative study of pitfalls in the FFT. *IEEE Transactions on Aerospace and Electronic Systems*, 16, 434–439. <https://doi.org/10.1109/taes.1980.308971>
- Glassmeier, K. H., Auster, H. U., Heyner, D., Okrafka, K., Carr, C., Berghofer, G., et al. (2010). The fluxgate magnetometer of the BepiColombo Mercury Planetary Orbiter. *Planetary and Space Science*, 58, 287–299. <https://doi.org/10.1016/j.pss.2008.06.018>
- Grundy, W. M., Young, L. A., Spencer, J. R., Johnson, R. E., Young, E. F., & Buie, M. W. (2006). Distributions of H<sub>2</sub>O and CO<sub>2</sub> ices on Ariel, Umbriel, Titania, and Oberon from IRTF/SpEx observations. *Icarus*, 184, 543–555. <https://doi.org/10.1016/j.icarus.2006.04.016>
- Hand, K. P., & Chyba, C. F. (2007). Empirical constraints on the salinity of the european ocean and implications for a thin ice shell. *Icarus*, 189, 424–438. <https://doi.org/10.1016/j.icarus.2007.02.002>
- Herbert, F. (2009). Aurora and magnetic field of Uranus. *Journal of Geophysical Research*, 114, A11206. <https://doi.org/10.1029/2009ja014394>
- Hofstadter, M., & Simon, A. (2017). *Ice Giants: Pre-Decadal Survey Mission Study Report*. Pasadena, CA: Jet Propulsion Laboratory. Report JPL D-100520.
- Husmann, H., Sohl, F., & Spohn, T. (2006). Subsurface oceans and deep interiors of medium-sized outer planet satellites and large trans-neptunian objects. *Icarus*, 185, 258–273. <https://doi.org/10.1016/j.icarus.2006.06.005>
- Husmann, H., Sotin, C., & Lunine, J. I. (2015). Interiors and evolution of icy satellites. In G. Schubert (Ed.), *Treatise on Geophysics* (2nd ed., pp. 605–635). Amsterdam. <https://doi.org/10.1016/b978-0-444-53802-4.00178-0>

- Ida, S., Ueta, S., Sasaki, T., & Ishizawa, Y. (2020). Uranian satellite formation by evolution of a water vapour disk generated by a giant impact. *Nature Astronomy*, 4, 880–885. <https://doi.org/10.1038/s41550-020-1049-8>
- Jackson, J. D. (1999). *Classical Electrodynamics* (3rd ed.). New York: Wiley.
- JPL Solar System Dynamics. (2021). Retrieved from [https://ssd.jpl.nasa.gov/?sat\\_elem](https://ssd.jpl.nasa.gov/?sat_elem)
- Kamata, S., Nimmo, F., Sekine, Y., Kuramoto, K., Noguchi, N., Kimura, J., & Tani, A. (2019). Pluto's ocean is capped and insulated by gas hydrates. *Nature Geoscience*, 12, 407–410. <https://doi.org/10.1038/s41561-019-0369-8>
- Kegerreis, J. A., Teodoro, L. F. A., Eke, V. R., Massey, R. J., Catling, D. C., Fryer, C. L., et al. (2018). Consequences of giant impacts on early Uranus for rotation, internal structure, debris, and atmospheric erosion. *The Astrophysical Journal*, 861, 52. <https://doi.org/10.3847/1538-4357/aae725>
- Khurana, K. K., Kivelson, M. G., Hand, K. P., & Russell, C. T. (2009). Electromagnetic induction from Europa's ocean and the deep interior. In R. T. Pappalardo, W. B. McKinnon, & K. Khurana (Eds.), *Europa* (pp. 571–586). Tucson, AZ: University of Arizona Press.
- Kivelson, M. G., Khurana, K. K., Means, J. D., Russell, C. T., & Snare, R. C. (1992). The Galileo magnetic field investigation. *Space Science Reviews*, 60, 357–383. [https://doi.org/10.1007/978-94-011-2512-3\\_15](https://doi.org/10.1007/978-94-011-2512-3_15)
- Morbidelli, A., Tsiganis, K., Batygin, K., Crida, A., & Gomes, R. (2012). Explaining why the uranian satellites have equatorial prograde orbits despite the large planetary obliquity. *Icarus*, 219, 737–740. <https://doi.org/10.1016/j.icarus.2012.03.025>
- Neveu, M., & Rhoden, A. R. (2019a). Evolution of Saturn's mid-sized moons. *Nature Astronomy*, 3, 543–552. <https://doi.org/10.1038/s41550-019-0726-y>
- Neveu, M., & Rhoden, A. R. (2019b). *Origin and evolution of Saturn's mid-sized moons*. EPSC Abstract. EPSC-DPS2019-2713.
- Nimmo, F., & Pappalardo, R. T. (2016). Ocean worlds in the outer solar system. *Journal of Geophysical Research*, 121, 1378–1399. <https://doi.org/10.1002/2016je005081>
- Parkinson, W. D. (1983). *Introduction to Geomagnetism*. Edinburgh: Scottish Academic Press.
- Paty, C., Arridge, C. S., Cohen, I. J., DiBraccio, G., Ebert, R. W., & Rymer, A. M. (2020). Ice giant magnetospheres. *Philosophical Transactions of the Royal Society of London - A*, 378, 20190480. <https://doi.org/10.1098/rsta.2019.0480>
- Raymond, C. A., Jia, X., Joy, S. P., Khurana, K. K., Murphy, N., Russell, C. T., et al. (2015). *Interior Characterization of Europa using Magnetometry (ICEMAG): Probing the European ocean and exosphere*. Fall AGU Meeting. abstract P13E-08.
- Rebello, L. R. B., Siepmann, T., & Drexler, S. (2020). Correlations between TDS and electrical conductivity for high-salinity formation brines characteristic of South Atlantic pre-salt basins. *WaterSA*, 46, 602–609. <https://doi.org/10.17159/wsa/2020.v46.i4.9073>
- Rogoszinski, Z., & Hamilton, D. P. (2021). Tilting Uranus: Collisions versus spin–orbit resonance. *The Planetary Science Journal*, 2, 78. <https://doi.org/10.3847/psj/abec4e>
- Safronov, V. S. (1966). Sizes of the largest bodies falling onto the planets during their formation. *Soviet Astronomy*, 9, 987–991.
- Schenk, P. M. (1991). Fluid volcanism on Miranda and Ariel: Flow morphology and composition. *Journal of Geophysical Research*, 96, 1887–1906. <https://doi.org/10.1029/90jb01604>
- Schenk, P. M., & Moore, J. M. (2020). Topography and geology of Uranian mid-sized icy satellites in comparison with Saturnian and Plutonian satellites. *Philosophical Transactions of the Royal Society of London - A*, 378, 20200102. <https://doi.org/10.1098/rsta.2020.0102>
- Schmidt, C., & Manning, C. (2017). Pressure-induced ion pairing in MgSO<sub>4</sub> solutions: Implications for the oceans of icy worlds. *Geochemical Perspectives Letters*, 3, 66–74. <https://doi.org/10.7185/geochemlet.1707>
- Seufert, M., Saur, J., & Neubauer, F. M. (2011). Multi-frequency electromagnetic sounding of the Galilean moons. *Icarus*, 211, 477–494. <https://doi.org/10.1016/j.icarus.2011.03.017>
- Slattery, W. L., Benz, W., & Cameron, A. G. W. (1991). Giant impacts on a primitive Uranus. *Icarus*, 99, 167–174.
- Smith, S. H. (1962). Temperature correction in conductivity measurements. *Limnology & Oceanography*, 7, 330–334. <https://doi.org/10.4319/lo.1962.7.3.0330>
- Srivastava, S. P. (1966). Theory of the magnetotelluric method for a spherical conductor. *Geophysical Journal of the Royal Astronomical Society*, 11, 373–387. <https://doi.org/10.1111/j.1365-246x.1966.tb03090.x>
- Szulágyi, J., Cilibrasi, M., & Mayer, L. (2018). In situ formation of icy moons of Uranus and Neptune. *The Astrophysical Journal Letters*, 868, L13. <https://doi.org/10.3847/2041-8213/aaced6>
- The Navigation and Ancillary Information Facility. (2021). Retrieved from <https://naif.jpl.nasa.gov/naif/spiceconcept.html>
- Tittmore, W. C. (1990). Tidal heating of Ariel. *Icarus*, 87, 110–139. [https://doi.org/10.1016/0019-1035\(90\)90024-4](https://doi.org/10.1016/0019-1035(90)90024-4)
- Weiss, B. P., Biersteker, J. B., Colicci, V., Couch, A., Petropoulos, A., & Balint, T. (2021). Searching for subsurface oceans on the moons of Uranus. In *Lunar and Planetary Science Conference*, LII. abstract #2096.
- Weiss, B. P., Colicci, V., & Biersteker, J. B. (2020). *Searching for subsurface oceans on the moons of Uranus*. AGU Fall Meeting. abstract #P074-007.
- Widemann, T., Sicardy, B., Dusser, R., Martinez, C., Beisker, W., Bredner, E., et al. (2009). Titania's radius and an upper limit on its atmosphere from the September 8, 2001 stellar occultation. *Icarus*, 199, 458–476.
- Zahnle, K., Schenk, P., Levison, H., & Dones, L. (2003). Cratering rates in the outer Solar System. *Icarus*, 163, 263–289. [https://doi.org/10.1016/s0019-1035\(03\)00048-4](https://doi.org/10.1016/s0019-1035(03)00048-4)
- Zimmer, C., Khurana, K. K., & Kivelson, M. G. (2000). Subsurface oceans on Europa and Callisto: Constraints from Galileo magnetometer observations. *Icarus*, 147, 329–347. <https://doi.org/10.1006/icar.2000.6456>

## Erratum

In the originally published version of this article, the driving frequencies used to calculate Figures 4 and S4 were a factor of  $2\pi$  too low due to a coding error in converting from period to angular frequency. The figures have since been corrected, and the present version may be considered the authoritative version of record.